

LETTERS

Longitudinal unzipping of carbon nanotubes to form graphene nanoribbons

Dmitry V. Kosynkin¹, Amanda L. Higginbotham¹, Alexander Sinitskii¹, Jay R. Lomeda¹, Ayrat Dimiev¹, B. Katherine Price¹ & James M. Tour^{1,2,3}

Graphene, or single-layered graphite, with its high crystallinity and interesting semimetal electronic properties, has emerged as an exciting two-dimensional material showing great promise for the fabrication of nanoscale devices^{1–3}. Thin, elongated strips of graphene that possess straight edges, termed graphene ribbons, gradually transform from semiconductors to semimetals as their width increases^{4–7}, and represent a particularly versatile variety of graphene. Several lithographic^{7,8}, chemical^{9–11} and synthetic¹² procedures are known to produce microscopic samples of graphene nanoribbons, and one chemical vapour deposition process¹³ has successfully produced macroscopic quantities of nanoribbons at 950 °C. Here we describe a simple solution-based oxidative process for producing a nearly 100% yield of nanoribbon structures by lengthwise cutting and unravelling of multiwalled carbon nanotube (MWCNT) side walls. Although oxidative shortening of MWCNTs has previously been achieved¹⁴, lengthwise cutting is hitherto unreported. Ribbon structures with high water solubility are obtained. Subsequent chemical reduction of the nanoribbons from MWCNTs results in restoration of electrical conductivity. These early results affording nanoribbons could eventually lead to applications in fields of electronics and composite materials where bulk quantities of nanoribbons are required^{15–17}.

We obtained oxidized nanoribbons by suspending MWCNTs in concentrated sulphuric acid followed by treatment with 500 wt% KMnO₄ for 1 h at room temperature (22 °C) and 1 h at 55–70 °C (Methods). After isolation, the resulting nanoribbons were highly soluble in water (12 mg ml⁻¹), ethanol and other polar organic solvents. The opening of the nanotubes appears to occur along a line, similar to the ‘unzipping’ of graphite oxide^{18,19}, affording straight-edged ribbons. This could occur in a linear longitudinal cut (Fig. 1a) or in a spiralling manner, depending upon the initial site of attack and the chiral angle of the nanotube. Although depicted in Fig. 1a as occurring on the mid-section of the nanotube rather than at one end, the location of the initial attack is not known.

The mechanism of opening is based on previous work on the oxidation of alkenes by permanganate in acid. The proposed first step in the process is manganate ester formation (2, Fig. 1b) as the rate-determining step, and further oxidation is possible to afford the dione (3, Fig. 1b) in the dehydrating medium²⁰. Juxtaposition of the buttressing ketones distorts the β,γ -alkenes (red in 3), making them more prone to the next attack by permanganate. As the process continues, the buttressing-induced strain on the β,γ -alkenes lessens because there is more space for carbonyl projection; however, the bond-angle strain induced by the enlarging hole (or tear if originating from the end of the nanotube) would make the β,γ -alkenes (4, Fig. 1b) increasingly reactive. Hence, once an opening has been initiated, its further opening is enhanced relative to an unopened tube or to an

uninitiated site on the same tube. The ketones can be further converted, through their O-protonated forms, to the carboxylic acids²¹ that will line the edges of the nanoribbons. Finally, relief of the bond-angle strain when the nanotube opens to the graphene ribbon (5, Fig. 1b) slows further dione formation and cutting²⁰. Thus, the preference for sequential bond cleavage over random opening and subsequent cutting, as occurs with nitric acid oxidation, can be explained by concerted attachment to neighbouring carbon atoms by permanganate, contrasting with the random attack on non-neighbouring carbon atoms by the nitronium species from nitric acid. The surface of the now-less-strained nanoribbon remains prone to 1,2-diol formation, which leads to the overall highly oxidized ribbon, but this is less likely to result in further oxidative cutting to the dione owing to relief of the tubular strain on the double bonds.

We achieved the same unzipping process in single-walled carbon nanotubes (SWCNTs), to produce narrow nanoribbons, but their subsequent disentanglement is more difficult. See Supplementary Figs 5 and 6 for images and analysis of those SWCNT-derived narrow nanoribbons and their reduction products.

We used transmission electron microscopy (TEM), atomic force microscopy (AFM) and scanning electron microscopy (SEM) to image the ribbon structures. TEM analysis shows nanoribbons (Fig. 1c) produced from MWCNTs with a starting diameter of 40–80 nm and approximately 15–20 inner nanotube layers (additional TEM images of untreated MWCNTs can be found in the Supplementary Fig. 1a, b). After reaction, the width of the carbon nanostructures increased to >100 nm and they had linear edges with little pristine MWCNT side-wall structure remaining (see Supplementary Figs 1 and 2 for more images). The MWCNTs used were produced from a chemical vapour deposition process²²; we attempted the same H₂SO₄–KMnO₄ treatment on a single sample of laser-oven-produced MWCNTs, but fewer nanoribbon-like structures were detected. AFM imaging (Fig. 1d) shows the presence of single atomic layers after tip sonication of the solution for 30 min to yield well-dispersed and sonication-shortened ribbons suitable for imaging. SEM imaging (Fig. 1e) of nanoribbons on a silicon surface shows that the ribbons remain long (~4 μ m in this image) when not cut by tip sonication; they can be dispersed as single or thin layers and they display uniform widths and predominantly straight edges over their entire length (see Supplementary Fig. 1c, d for other images).

The degree of consecutive tube opening in the MWCNTs can also be controlled by adjusting the amount of oxidizing agent introduced into the system; using TEM, we found that in 80–100% of the MWCNTs present, the side walls completely unravelled to form nanoribbons when 500 wt% KMnO₄ was used. The successive opening reaction was demonstrated in five iterations, each containing a stepwise increase in the amount of KMnO₄: 100 wt% KMnO₄ in the

¹Department of Chemistry, ²Department of Mechanical Engineering and Materials Science, ³Smalley Institute for Nanoscale Science and Technology, Rice University, MS-222, 6100 Main Street, Houston, Texas 77005, USA.

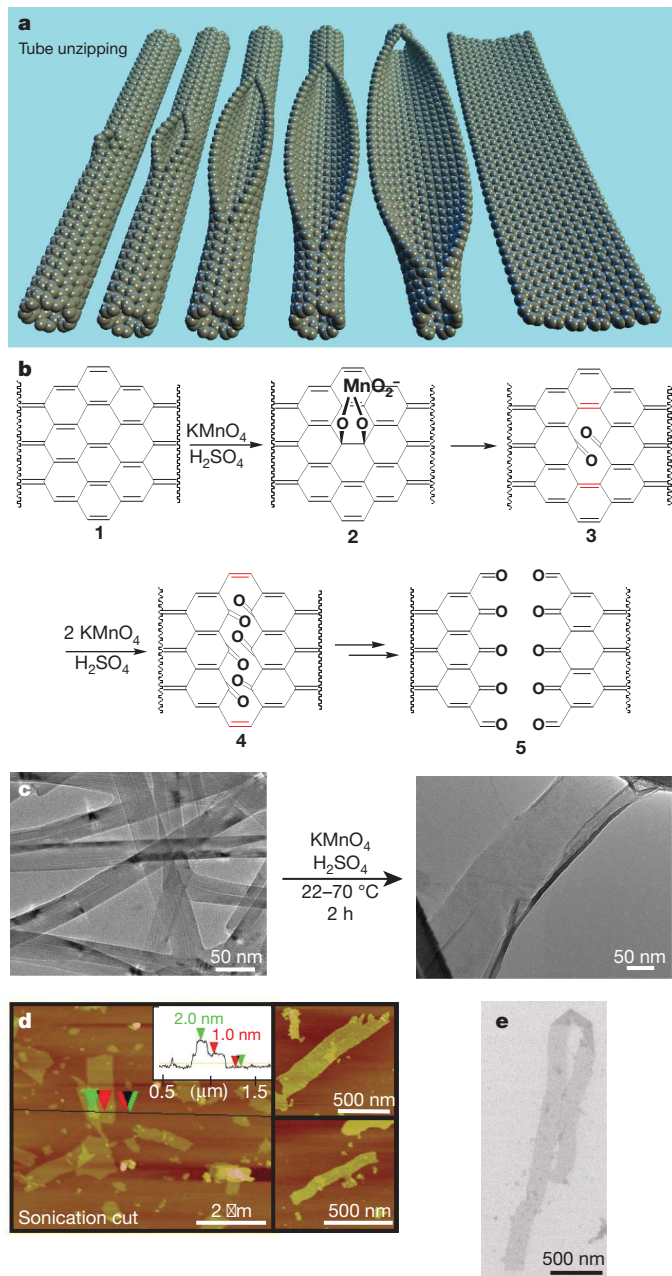


Figure 1 | Nanoribbon formation and imaging. **a**, Representation of the gradual unzipping of one wall of a carbon nanotube to form a nanoribbon. Oxygenated sites are not shown. **b**, The proposed chemical mechanism of nanotube unzipping. The manganate ester in **2** could also be protonated. **c**, TEM images depicting the transformation of MWCNTs (left) into oxidized nanoribbons (right). The right-hand side of the ribbon is partly folded onto itself. The dark structures are part of the carbon imaging grid. **d**, AFM images of partly stacked multiple short fragments of nanoribbons that were horizontally cut by tip-ultrasonic treatment of the original oxidation product to facilitate spin-casting onto the mica surface. The height data (inset) indicates that the ribbons are generally single layered. The two small images on the right show some other characteristic nanoribbons. **e**, SEM image of a folded, 4- μm -long single-layer nanoribbon on a silicon surface.

first iteration (sample I), 200 wt% in the second iteration (sample II), and so on until the final iteration, when we used 500 wt% (sample V). This resulted in consecutive unencapsulation of the different layers by unzipping of the successive MWCNTs (see Methods for details). It is evident from TEM images (Fig. 2a–e) that the walls of the MWCNTs open to a higher degree as the level of oxidation increases, with less MWCNT inner tube remaining in successive iterations. This is highlighted in a statistical plot (Fig. 2f) showing the decrease of the

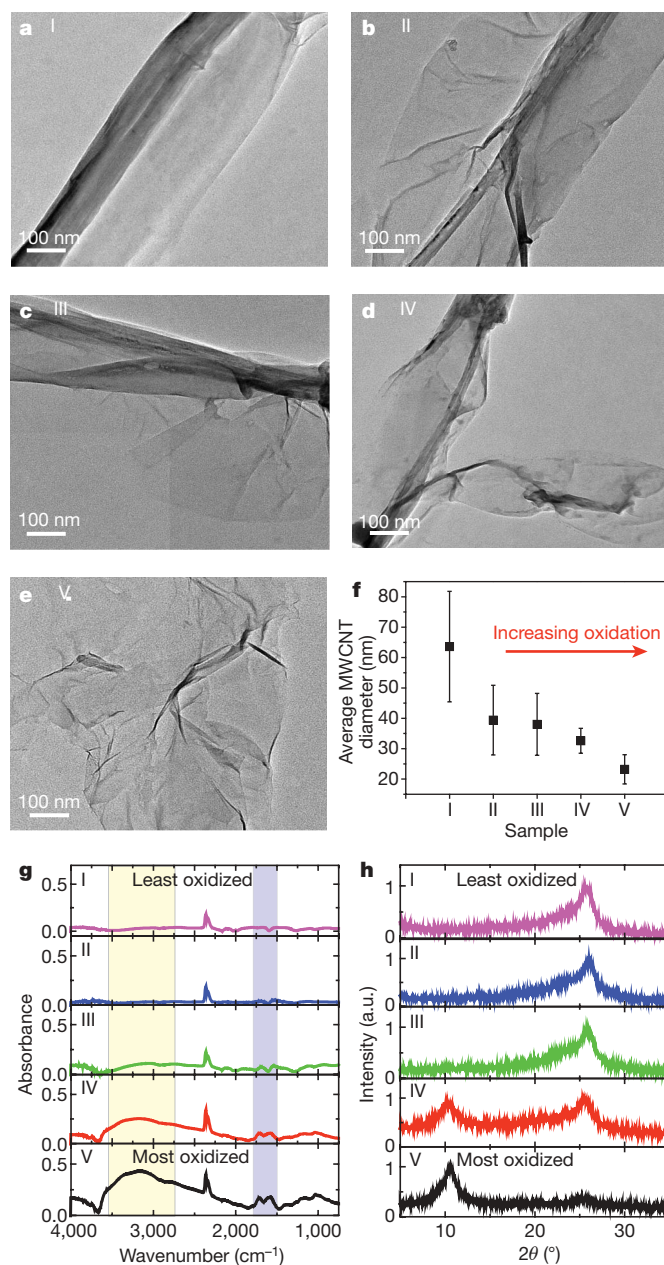


Figure 2 | Stepwise opening of MWCNTs to form nanoribbons. **a–e**, TEM images of the stepwise opening of MWCNTs representing the incremental exposure of the system to KMnO_4 ; the least oxidized sample (sample I) is in **a** and the most oxidized sample (sample V) is in **e**. **f**, Scatter plot showing how the average MWCNT diameter (determined from studying 15–20 TEM images per sample, each with ~ 5 MWCNTs per image) changes with increasing exposure to KMnO_4 . Error bars indicate the standard deviation of the average MWCNT diameter across the sample. **g**, ATR-IR spectroscopy of stepwise opening/oxidation of MWCNTs. **h**, X-ray diffraction analysis of the stepwise opening of the nanotube. θ , diffraction angle; a.u., arbitrary units.

average diameter of remaining MWCNTs from ~ 65 nm to ~ 20 nm as the amount of KMnO_4 exposure is increased. The smaller-diameter tubes that remained after treatment with 500 wt% KMnO_4 were exposed to the reaction conditions for less time than the larger-diameter tubes and, thus, may not have had the chance to fully react; no difference in the rate of unzipping between smaller- and larger-diameter nanotubes can be inferred from this data.

The degree of oxidation of the product formed (partly and/or completely unravelled MWCNTs) from each of the five iterative KMnO_4 treatment steps was monitored using attenuated-total-reflection infrared (ATR-IR) spectroscopy and thermogravimetric

analysis (TGA). ATR-IR spectroscopy (Fig. 2g) reveals the appearance of a C=O stretch (purple region, Fig. 2g) increasing from $1,690\text{ cm}^{-1}$ in sample III (green line) to $1,710\text{ cm}^{-1}$ in sample V (black line), consistent with declining conjugation. The COO-H/O-H stretch ($\sim 3,600\text{--}2,800\text{ cm}^{-1}$; yellow region, Fig. 2g) appears with sample III and continues to increase through the series, indicating an increase in the number of carboxyl and hydroxyl functionalities as well as the possible presence of trapped water. TGA shows an increase in the total weight loss (20% and 49% in samples I and V, respectively) with increasing exposure to KMnO_4 , implying an increase in the number of volatile side-wall functionalities present, which corroborates there being a higher degree of oxidation (Supplementary Fig. 3a). Furthermore, Raman spectroscopy (Supplementary Fig. 3b) shows an increasing level of disorder (appearance of a D band at $1,321\text{--}1,328\text{ cm}^{-1}$) with increasing oxidation, consistent with ATR-IR spectroscopy and TGA observations.

We also performed X-ray diffraction analysis (Fig. 2h), to investigate further the structure of the partly and completely unzipped MWCNT-nanoribbon structures. The graphite (002) spacing increases with the level of oxidation. Samples I-III all have 2θ values of $\sim 25.8^\circ$, corresponding to a d spacing of 3.4 \AA . Sample IV shows two peaks, one at 10.8° and one at 25.4° , with d spacings of 8.2 \AA and 3.5 \AA , respectively. Sample V shows a predominant peak at 10.6° , corresponding to a d spacing of 8.3 \AA , with minimal signal contributed by MWCNTs ($2\theta = 25.8^\circ$); this spectrum is very similar to that of graphite oxide (Supplementary Fig. 3c).

Both the nanoribbons and graphite oxide possess oxygen-containing functionalities such as carbonyls, carboxyls and hydroxyls²³ that have been shown to exist at the edges and the surface²⁴. The surface oxidation disrupts the π -conjugated network, rendering the nanoribbons and graphite oxide poorly conductive. Hydrazine (N_2H_4) reduction of graphite oxide²⁵ is known to provide a means of restoring conjugation and, thus, some of the conductivity, to form chemically converted graphene (CCG)²⁵⁻²⁸. The structure of CCG is thought to be a patchwork of intact graphene islands interspersed with regions of tetrahedral sp^3 -hybridized carbon atoms due to incomplete reduction and incomplete re-aromatization; therefore, the electrical conductivity is not as high as that found in the original graphite²⁶. The carboxyl groups, which are found predominately at the edges²⁵, are not reduced by N_2H_4 and remain in the product, further disrupting the π network^{7,8}. Furthermore, as the number of oxygen-containing functionalities decreases during the reduction process, the tendency to aggregate as a result of π stacking increases.

The reduction of oxidized nanoribbons was carried out with aqueous N_2H_4 in the presence of ammonia. To prevent re-aggregation during the reduction procedure, we first dispersed the nanoribbons in an

aqueous surfactant solution, sodium dodecyl sulphate (SDS), to produce stable dispersions of reduced nanoribbons that retained their straight-edged structure (Fig. 3a). The reaction progress was monitored by ultraviolet absorption (Fig. 3b); the bathochromic shift of λ_{max} and the hyperchromicity over the entire range ($>230\text{ nm}$) indicates that electronic conjugation of the ribbons was restored²⁵.

To provide further evidence that the reduction procedure decreased the number of oxygen-containing functionalities from the nanoribbon surface, we performed ATR-IR spectroscopy, X-ray photoemission spectroscopy (XPS; Fig. 3c, d) and TGA. The reduced nanoribbons show almost complete elimination of the COO-H/O-H stretching region ($\sim 3,600\text{--}2,800\text{ cm}^{-1}$; yellow region, Fig. 3c) and a significant decrease in the C=O stretching region ($\sim 1,710\text{ cm}^{-1}$; purple region, Fig. 3c) in the ATR-IR spectrum (blue line, Fig. 3c) in comparison with the intense COO-H/O-H and C=O stretches observed for the oxidized nanoribbons (red line, Fig. 3c). Edge carboxylic acids will remain.

In the XPS carbon 1s spectra of the oxidized and reduced nanoribbons (Fig. 3d), the signals at 286 eV and 287 eV correspond to C-O and C=O, respectively. The shoulder at 289 eV is assigned to carboxyl groups. Upon reduction (blue line), the 286- and 287-eV peaks diminish to a shoulder of the C-C peak (284.4 eV), indicating significant deoxygenation of the nanoribbons by N_2H_4 . As reported for CCG, the most dominant peak after reduction is the C-C peak at 284.8 eV (ref. 29). In addition, the XPS-determined atomic concentration of oxygen (complete table found in Supplementary Fig. 4b) decreases from 42% to 16% upon reduction, but is still higher than the oxygen content of MWCNTs (2.1%), owing, in large part, to the edge carboxylic acid moieties.

The TGA weight loss of the reduced nanoribbons was $\sim 33\%$ less than that of the oxidized starting material, which also indicates that fewer oxygen-containing functionalities are present on the nanoribbon surface (see Supplementary Fig. 4d for TGA curves). The TEM image of a reduced nanoribbon shows its straight edge and buckled appearance (Fig. 3a). Nitrogen adsorption measurements of as-prepared and reduced nanoribbons give surface areas, determined using Brunauer-Emmett-Teller theory, of 445 and $436\text{ m}^2\text{ g}^{-1}$, respectively, after pre-outgassing at 400°C for 12 h (ref. 13). The density of the oxidized ribbons was found to be 2.0 g cm^{-3} using solution density matching (bromotrichloromethane). When considering the overall conversion of MWCNTs to reduced nanoribbons, the material weight yield is 99% (Methods), underscoring the efficiency of the overall process.

Recent interest in graphene nanoribbons has focused on the study of the reactive edges having zigzag or armchair morphologies that dominate their electronic and magnetic behaviour⁵. Although zigzag-edged structures are presumed by the mechanism described

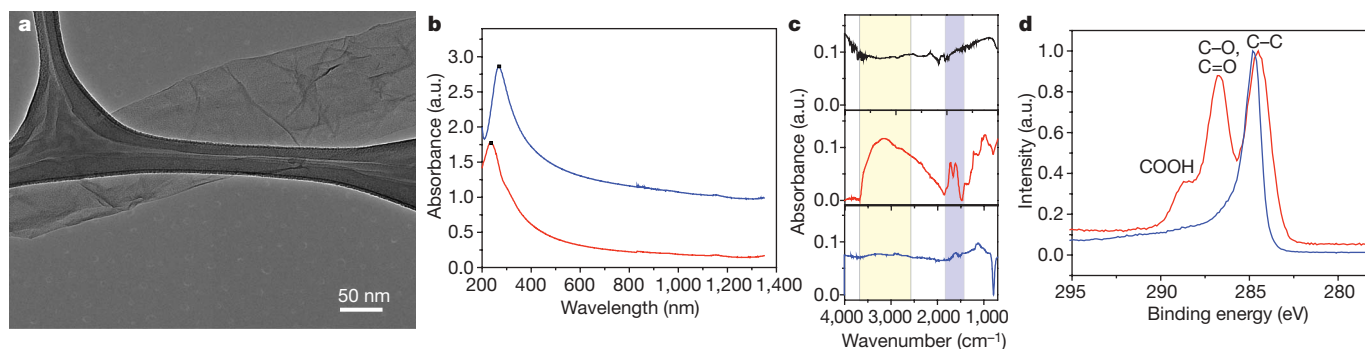


Figure 3 | Characterization of the oxidized and reduced nanoribbons derived from MWCNTs. **a**, TEM image of reduced nanoribbons obtained by treatment of oxidized nanoribbons with N_2H_4 . Detailed examination of the image reveals that 2–3 ribbons are stacked with apparent buckling. The dark structures are part of the carbon imaging grid. **b**, Changes in the ultraviolet spectrum of an aqueous solution of oxidized nanoribbons (red),

$\lambda_{\text{max}} = 234\text{ nm}$) after treatment with N_2H_4 (blue, $\lambda_{\text{max}} = 267\text{ nm}$). **c**, ATR-IR spectroscopy of nanoribbons before (red) and after reduction (blue), compared with MWCNT starting material (black). **d**, Normalized, superimposed XPS carbon 1s spectra of the oxidized nanoribbons (red) and the reduced nanoribbons (blue).

here, we were unable to achieve the edge resolution needed to confirm this. This is due, in part, to edge curling, and could be further attributed to the extensive edge oxidation; this may be removed only upon treatment at $\geq 2,000$ °C, which would result in reconstruction and modified electronic properties.

In spite of the oxidized edges and planes of the nanoribbons derived by this bulk process, the electronic properties of the nanoribbons before and after chemical reduction were studied by building three-terminal devices on Si–SiO₂ substrates. The long length of the nanoribbons make them easily adapted structures for device fabrication (Fig. 4a); electron-beam-patterned platinum electrodes were evaporated on top of the nanoribbon stack. As-prepared nanoribbons are poor conductors owing to the high number of oxygen-containing functionalities present on the surface; however, their conductivity can be dramatically increased either by chemical reduction using N₂H₄ or by annealing in H₂ (Fig. 4b). Thick nanoribbon stacks show little gate effect, which is in accord with previously reported data³⁰. Conversely, bilayers of these reduced graphene nanoribbons have field-effect properties with a minimum conductivity at zero gate voltage, which is as expected for undoped field-effect devices made from exfoliated graphene sheets and is superior to CCGs (Fig. 4c, d)^{2,30}. The conductivities obtained from these wide nanoribbons are analogous to device properties reported^{11,13} for other wide nanoribbons either exfoliated or grown by chemical vapour deposition. We have so far been unable to build acceptable devices from narrow nanoribbons derived from SWCNTs, owing to their extreme entanglement (Supplementary Fig. 5); moreover, edge oxidation in those small structures may retard their electronic utility. Although the preparative route described here can have the advantage of producing accessible nanoribbons on a large scale, these unzipping-derived nanoribbons, with their residual oxidized

defect sites, have electronic characteristics inferior to those of wide, mechanically peeled sheets of graphene^{2,30}.

METHODS SUMMARY

Nanoribbon formation. MWCNTs were used as received from Mitsui & Co. (lot no. 05072001K28). We suspended MWCNTs in concentrated sulphuric acid (H₂SO₄) for a period of 1–12 h and then treated them with 500 wt% potassium permanganate (KMnO₄). The H₂SO₄ conditions aid in exfoliating the nanotube and the subsequent graphene structures. The reaction mixture was stirred at room temperature for 1 h and then heated to 55–70 °C for an additional 1 h. When all of the KMnO₄ had been consumed, we quenched the reaction mixture by pouring over ice containing a small amount of hydrogen peroxide (H₂O₂). The solution was filtered over a polytetrafluoroethylene (PTFE) membrane, and the remaining solid was washed with acidic water followed by ethanol/ether.

Stepwise oxidation of MWCNTs to nanoribbons. We followed the above reaction procedure, except that 100 wt% KMnO₄ was added in portions until 500 wt% was achieved. When the KMnO₄ had been consumed at every step, a portion of the reaction solution was removed and worked up for analysis as described above.

Nanoribbon reduction. We treated a water solution (200 mg l⁻¹) of the above-isolated nanoribbons (with or without 1 wt% SDS surfactant) with 1 vol% concentrated ammonium hydroxide (NH₄OH) and 1 vol% hydrazine monohydrate (N₂H₄·H₂O). Before being heating to 95 °C for 1 h, the solution was covered with a thin layer of silicon oil.

Full Methods and any associated references are available in the online version of the paper at www.nature.com/nature.

Received 1 October 2008; accepted 11 February 2009.

- Geim, A. K. & Novoselov, K. S. The rise of graphene. *Nature Mater.* **6**, 183–191 (2007).
- Novoselov, K. S. *et al.* Two-dimensional gas of massless Dirac fermions in graphene. *Nature* **438**, 197–200 (2005).
- Zhang, Y., Tan, Y.-W., Stormer, H. L. & Kim, P. Experimental observation of the quantum Hall effect and Berry's phase in graphene. *Nature* **438**, 201–204 (2005).
- Areshkin, D. A., Gunlycke, D. & White, C. T. Ballistic transport in graphene nanostrips in the presence of disorder: importance of edge effects. *Nano Lett.* **7**, 204–210 (2007).
- Nakada, K., Fujita, M., Dresselhaus, G. & Dresselhaus, M. S. Edge state in graphene ribbons: nanometer size effect and edge shape dependence. *Phys. Rev. B* **54**, 17954–17961 (1996).
- Son, Y.-W., Cohen, M. L. & Louie, S. G. Energy gaps in graphene nanoribbons. *Phys. Rev. Lett.* **97**, 216803 (2006).
- Han, M. Y., Oezylmaz, B., Zhang, Y. & Kim, P. Energy band-gap engineering of graphene nanoribbons. *Phys. Rev. Lett.* **98**, 206805 (2007).
- Chen, Z., Lin, Y.-M., Rooks, M. J. & Avouris, P. Graphene nano-ribbon electronics. *Physica E* **40**, 228–232 (2007).
- Schniepp, H. C. *et al.* functionalized single graphene sheets derived from splitting graphite oxide. *J. Phys. Chem. B* **110**, 8535–8539 (2006).
- Rollings, E. *et al.* Synthesis and characterization of atomically thin graphite films on a silicon carbide substrate. *J. Phys. Chem. Solids* **67**, 2172–2177 (2006).
- Li, X., Wang, X., Zhang, L., Lee, S. & Dai, H. Chemically derived, ultrasmooth graphene nanoribbon semiconductors. *Science* **319**, 1229–1232 (2008).
- Yang, X. *et al.* Two-dimensional graphene nanoribbons. *J. Am. Chem. Soc.* **130**, 4216–4217 (2008).
- Campos-Delgado, J. *et al.* Bulk production of a new form of sp² carbon: crystalline graphene nanoribbons. *Nano Lett.* **8**, 2773–2778 (2008).
- Saito, T., Matsushige, K. & Tanaka, K. Chemical treatment and modification of multi-walled carbon nanotubes. *Physica B* **323**, 280–283 (2002).
- Son, Y.-W., Cohen, M. L. & Louie, S. G. Half-metallic graphene nanoribbons. *Nature* **444**, 347–349 (2006).
- Liang, G., Neophytou, N., Nikonov, D. E. & Lundstrom, M. S. Performance projections for ballistic graphene nanoribbon field-effect transistors. *IEEE Trans. Electron. Dev.* **54**, 677–682 (2007).
- Wang, X. *et al.* Room-temperature all-semiconducting sub-10-nm graphene nanoribbon field-effect transistors. *Phys. Rev. Lett.* **100**, 206803 (2008).
- Li, J.-L. *et al.* Oxygen-driven unzipping of graphitic materials. *Phys. Rev. Lett.* **96**, 176101 (2006).
- Ajayan, P. M. & Yakobson, B. I. Oxygen breaks into carbon world. *Nature* **441**, 818–819 (2006).
- Wolfe, S., Ingold, C. F. & Lemieux, R. U. Oxidation of olefins by potassium permanganate: mechanism of α -ketol formation. *J. Am. Chem. Soc.* **103**, 938–939 (1981).
- Banoo, F. & Stewart, R. Mechanisms of permanganate oxidation. IX. Permanganate oxidation of aromatic alcohols in acid solution. *Can. J. Chem.* **47**, 3199–3205 (1969).
- Endo, M. Grow carbon fibers in the vapor phase. *Chemtech* **18**, 568–576 (1988).
- Hummers, W. S. Jr & Offeman, R. E. Preparation of graphitic oxide. *J. Am. Chem. Soc.* **80**, 1339 (1958).
- Lerf, A., He, H., Forster, M. & Klinowski, J. Structure of graphite oxide revisited. *J. Phys. Chem. B* **102**, 4477–4482 (1998).

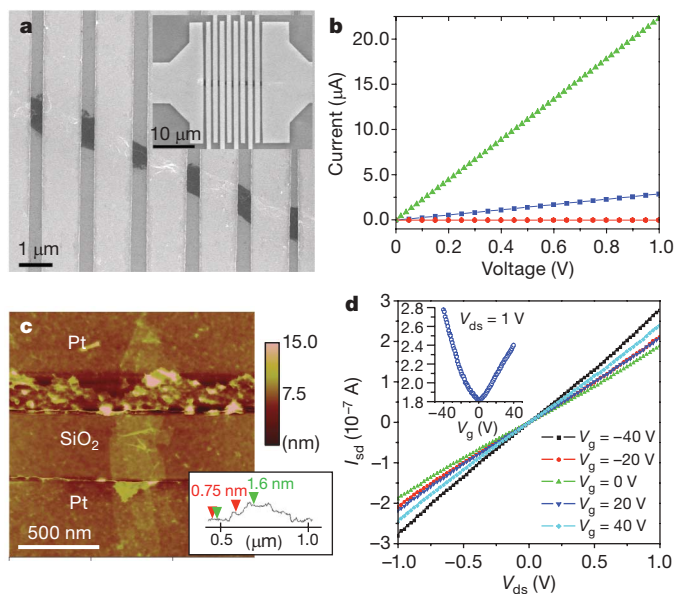


Figure 4 | Device fabrication and electrical properties of graphene nanoribbons on SiO₂-Si. **a**, SEM image of a multi-terminal device based on a multilayer (~10-nm-thick) stack of graphene nanoribbons with platinum electrodes. Inset, larger image of a similar device. **b**, Current–voltage curves for three different types of device: as-prepared (red), N₂H₄-reduced (blue) and H₂-annealed (green) nanoribbons (~300 nm wide, 10 nm thick (AFM) with a channel length of ~500 nm; characteristic of the >10 devices measured for each of the three states). **c**, AFM image of another device based on a N₂H₄-reduced and annealed (H₂/Ar at 300 °C for 10 min) bilayer nanoribbon showing that the ribbon consists of two overlapping nanoribbons in the SiO₂ channel region. Typical height profile (inset) across this nanoribbon shows steps of about 0.75 nm, which correspond to individual graphene sheets. These sheets overlap in the middle, resulting in a height of ~1.6 nm. **d**, Source–drain current (I_{sd}), source–drain voltage (V_{ds}) and gate voltage (V_g) dependencies for the device shown in **c**; p-doped silicon was used as a back gate.

25. Li, D., Mueller, M. B., Gilje, S., Kaner, R. B. & Wallace, G. G. Processable aqueous dispersions of graphene nanosheets. *Nature Nanotechnol.* **3**, 101–105 (2008).
26. Stankovich, S. *et al.* Synthesis of graphene-based nanosheets via chemical reduction of exfoliated graphite oxide. *Carbon* **45**, 1558–1565 (2007).
27. Bourlino, A. B. *et al.* Graphite oxide: chemical reduction to graphite and surface modification with primary aliphatic amines and amino acids. *Langmuir* **19**, 6050–6055 (2003).
28. Eda, G., Fanchini, G. & Chhowalla, M. Large-area ultrathin films of reduced graphene oxide as a transparent and flexible electronic material. *Nature Nanotechnol.* **3**, 270–274 (2008).
29. Stankovich, S. *et al.* Stable aqueous dispersions of graphitic nanoplatelets via the reduction of exfoliated graphite oxide in the presence of poly(sodium 4-styrenesulfonate). *J. Mater. Chem.* **16**, 155–158 (2006).
30. Novoselov, K. S. *et al.* Electric field effect in atomically thin carbon films. *Science* **306**, 666–669 (2004).

Supplementary Information is linked to the online version of the paper at www.nature.com/nature.

Acknowledgements The authors thank P. M. Ajayan, W. Guo, J. Duque, Z. Sun, and Z. Jin for technical assistance and discussions. Mitsui & Co. generously donated the MWCNTs. The work was funded by the US Defense Advanced Research Projects Agency, the US Federal Aviation Administration, Department of Energy (DE-FC-36-05GO15073) and Wright Patterson Air Force Laboratory through the US Air Force Office of Scientific Research.

Author Contributions D.V.K. discovered the unzipping reaction and made most of the analysed ribbons. A.L.H. obtained and analysed most of the analysis data including the TEM, AFM, ultraviolet, XPS, TGA, Raman and infrared data; she also made some of the ribbons and wrote the majority of the manuscript. A.S. fabricated and tested the electronic devices. J.R.L. performed some of the spectral analysis including the X-ray diffraction. A.D. prepared and studied the nanoribbons on silicon surfaces for electrical analysis. B.K.P. performed some of the AFM analyses. J.M.T. oversaw and directed all aspects of the syntheses, data analysis and manuscript correction and finalization.

Author Information Reprints and permissions information is available at www.nature.com/reprints. Correspondence and requests for materials should be addressed to J.M.T. (tour@rice.edu).

METHODS

MWCNTs were used as received from Mitsui & Co. (lot no. 05072001K28). The remaining chemicals were purchased from Sigma-Aldrich and used as received, except for the concentrated sulphuric acid (Fisher Scientific). Deionized water (18-M Ω resistivity) obtained from a NanoPure system (Barnstead) was used throughout this work.

Nanoribbon formation. In a typical procedure, MWCNTs (150 mg, 12.5 mequiv. carbon) were suspended in 150 ml of concentrated H₂SO₄ for 1 h to 12 h. KMnO₄ (750 mg, 4.75 mmol) was then added and the mixture allowed to stir for 1 h at room temperature. The reaction was then heated in an oil bath at 55 °C for 30 min. The progress of the reaction was monitored by preparing two test tubes, one containing 1 ml of deionized water and 2–3 drops of hydrogen peroxide (30%), and one containing 1 ml of water only. Four or five drops of the reaction mixture were added to the test tubes and bath-sonicated for 3 min. The colour and dispersibility of the solution in the test tube containing the hydrogen peroxide was noted; if the solution was yellow/brown and the solid broke up into very small pieces, the reaction was complete. The other test tube was used to check the level of permanganate consumption; if a dark purple/blue hue was observed (like that seen when KMnO₄ is dissolved in water), the reaction was not complete. Alternatively, a solution with a red hue signified the presence of manganese(IV), indicating permanganate consumption and a complete reaction. It was also important to note the colour of the reaction mixture itself; the colour went from black to dark brown with the green colour of permanganate in acid disappearing by reaction completion. If the reaction had not completed after 30 min at 55 °C, the temperature was increased to 65 °C. When the reaction temperature stabilized to 65 °C, the reaction status was checked again using the above test-tube procedure. Continued heating at 65 °C was needed if the permanganate was not entirely consumed.

When the reaction appeared nearly complete or complete, the temperature was increased to 70 °C and the solution was allowed to stabilize. Upon stabilization to 70 °C, the reaction was removed from the heat source, allowed to cool to room temperature and poured onto 400 ml of ice containing 5 ml of 30% H₂O₂ (to prevent precipitation of insoluble MnO₂). After vacuum filtration through a PTFE membrane (5.0- μ m pore size), the solid was removed and stirred in 150 ml of water for 30 min, and then bath-sonicated (Cole Parmer ultrasonic cleaner, Model 08849-00) for 15 min. The material was then flocculated by addition of 20 vol% concentrated HCl (30 ml). The solid was then filtered through a PTFE membrane (0.45- μ m pore size). The product was removed and stirred in 150 ml of ethanol for 30 min, then bath-sonicated (device as above) for 15 min. The material was flocculated by addition of 100 vol% ether (150 ml) followed by filtration through a PTFE membrane (0.45- μ m pore size). The final product was washed twice with ether (50 ml each time) and dried *in vacuo* to afford 321 mg of oxidized nanoribbons. Shortened ribbons (Fig. 1d) were formed from an aqueous solution of washed nanoribbons that were tip-sonicated at 30-W power (Misonix Sonicator 3000) for a total of 30 min (2 min on and 1 min off, for a total on-time of 30 min).

Stepwise oxidation. The stepwise oxidation was performed by first running the reaction, under the conditions specified above, with a 1:1 mass ratio of KMnO₄:MWCNT (denoted sample I, least oxidized). After 1 h at 55 °C, approximately one-fifth of the volume of the reaction mixture was extracted and worked up as outlined above. The remaining portion was then treated with 100 wt% KMnO₄ (relative to the portion of MWCNTs remaining) and allowed to react for

another 1 h at 55 °C. After extracting one-quarter of the volume of the reaction mixture, to be worked up, the rest was treated again with 100 wt% KMnO₄. The process was repeated until the final batch of ribbons was exposed to a total of 500 wt% KMnO₄ (denoted sample V, most oxidized; Fig. 2e).

Reduction of nanoribbons. Reduction in aqueous N₂H₄ can be done with or without SDS surfactant. To introduce the SDS surfactant, 50 mg of the as-prepared nanoribbons were homogenized (IKA T-25 digital ULTRA-TURRAX disperser with 18 G dispersing element, 7,000 r.p.m.) in 250 ml of 1% aqueous SDS solution for 1 h. The suspension was then cup-sonicated (Cole Parmer ultrasonic processor, 75% power) for 10 min and filtered through a 5-cm plug of glass wool. If SDS was not present, 50 mg of as-prepared nanoribbons was dissolved in 250 ml nanopure water. In both cases, 150 ml of the nanoribbon solution was covered by a 5-mm layer of silicon oil in an Erlenmeyer flask. To this solution we added 150 μ l of concentrated NH₄OH (2.22 mmol), followed by 150 μ l of N₂H₄·H₂O (98%, 3.03 mmol). The oil was added to eliminate the air–water interface that causes agglomeration of the reduced ribbons as water evaporates²⁵. The reaction mixture was heated at 95 °C for 1 h in a gently boiling water bath (no stirring). Excess N₂H₄ was removed by dialysis (CelluSep H1 regenerated cellulose tubular membrane; nominal molecular weight, 5,000 (relative molecular mass); 400-mm width) for 24 h in 1% NH₄OH. Filtering and drying *in vacuo* afforded 23.2 mg of reduced nanoribbons. Therefore, the overall weight conversion efficiencies from MWCNTs to the reduced nanoribbons were 215% and 46% for the two steps, yielding 99%.

Device fabrication. Fabrication of graphene devices was performed by tracking individual nanoribbons on the surface of highly doped Si substrates, covered with 200-nm-thick dielectric SiO₂, by SEM (JEOL-6500 microscope), followed by patterning of 20-nm-thick Pt contacts by standard electron beam lithography. Before being tested, the devices used to produce the data in Fig. 4d were annealed in H₂/Ar (1:1, <1 atm) atmosphere at 300 °C for 10 min. The electrical properties were tested using a probe station (Desert Cryogenics TT-probe 6 system) under vacuum with a chamber base pressure below 10⁻⁵ mm Hg. The current–voltage data were collected using an Agilent 4155C semiconductor parameter analyser.

Sample analysis. TEM imaging was performed on a JEOL-2010 microscope. Samples were prepared by dispersing the nanoribbons in a 1:1 ethanol:water mixture and dropped onto 300 mesh holey, lacey carbon grids on copper support (Ted Pella). AFM images were obtained with a Nanoscope IIIa (Digital Instruments/Veeco Metrology), operating in tapping mode, using Si tips n-doped with 1–10 Ω cm phosphorus (Veeco, MPP-11100-140) at a scan rate of 2 Hz and a resolution of 512 \times 512. Samples for AFM analysis were prepared by spin-coating aqueous solutions of nanoribbons at 3,000 r.p.m. onto a freshly cleaved mica surface (Ted Pella) and rinsed with deionized water and 2-isopropanol.

Ultraviolet–visible spectra were obtained on a Shimadzu UV-3101 PC with samples contained in 1-ml quartz cuvettes. Fourier-transform infrared spectroscopy was performed using a Nicolet FTIR Infrared Microscope with an ATR attachment. XPS was performed on a PHI Quantera SXM scanning X-ray microprobe with a pass energy of 26.00 eV, 45° take-off angle and a 100- μ m beam size. TGA (Q50, TA Instruments) was performed from room temperature to 950 °C at 10 °C min⁻¹ under argon. Raman spectroscopy was performed on a Renishaw Raman scope using a 633-nm HeNe laser. The X-ray diffraction measurements were carried out with a Rigaku diffractometer (Cu K α radiation; X-ray wavelength, λ = 1.5406 Å; operating energy, 40 keV; cathode current, 40 mA; scan rate, 1° min⁻¹). Brunauer–Emmett–Teller surface-area analysis was performed at 77 K on a Quantachrome Autosorb-1 Physisorption system using N₂ as the sorption gas.